processes

MDPI

Article

Adsorptive Removal of Oxygenated Organosulfur Compounds from Peroxymonosulfate-Treated Waters Using Micron-Sized Amorphous ZrO_x

Jia Xu [1], Wei Qiu [1,*] and Jingjing Yao [2]

[1] State Key Laboratory of Urban-Rural Water Resources and Environment, Harbin Institute of Technology, Harbin 150090, China; 22b929027@stu.hit.edu.cn
[2] Center for Environment and Water Resources, College of Chemistry and Chemical Engineering, Central South University, Changsha 410083, China; yaojj0412@163.com
* Correspondence: qiuwei@hit.edu.cn

Abstract

Oxygenated organosulfur compounds are oxygen-containing organic sulfur species, including organosulfates, sulfonates, and other sulfur-containing oxidation products. These compounds can persist after peroxymonosulfate (PMS) oxidation, yet their subsequent removal remains poorly understood. Here, micron-sized amorphous ZrO_x (MA-ZrO_x) was evaluated as an adsorbent for post-PMS treatment. In model-compound experiments at an initial concentration of 100 ng/L, five of seven representative compounds achieved removal efficiencies of at least 98% within 10 min. Density functional theory (DFT) calculations suggested that multiple hydrogen-bonding contacts and steric accessibility contributed to compound-dependent adsorption. In natural organic matter (NOM)-simulated water and two natural waters, MA-ZrO_x adsorption after PMS oxidation removed 37.8–54.3% of residual total organic carbon, accompanied by a decrease in the number of detected oxygenated organosulfur formulas. Fourier transform ion cyclotron resonance mass spectrometry (FT-ICR MS) revealed that O-rich N-free formulas showed higher apparent capture than the reference group (O = 4, N = 0), while N-containing groups showed higher pooled capture across the three waters. Exact formula-pair comparisons further indicated that CH_2 increments were associated with an initial decrease in apparent capture followed by a recovery. These findings support MA-ZrO_x adsorption as a complementary treatment step for controlling residual oxygenated organosulfur compounds after PMS oxidation.

Keywords: oxygenated organosulfur compounds; zirconium oxide; peroxymonosulfate; adsorption; hydrogen bonding; FT-ICR MS

Check for updates

Academic Editor: Maria Jose Martin de Vidales

Received: 13 September 2026
Revised: 13 October 2026
Accepted: 15 October 2026
Published: 18 October 2026

Copyright: © 2026 by the authors. Licensee MDPI, Basel, Switzerland. This article is an open access article distributed under the terms and conditions of the Creative Commons Attribution (CC BY) license.

1. Introduction

Persulfate-based advanced oxidation processes using peroxymonosulfate (PMS) or peroxydisulfate (PDS) have been widely investigated for the removal of refractory organic contaminants. These processes involve metal- or mineral-mediated, photochemical, or thermal activation to generate reactive oxidizing species [1–3]. Related applications have extended to pilot-scale wastewater treatment and field-scale groundwater remediation [4,5]. However, the disappearance of a target contaminant does not necessarily imply complete mineralization. Persulfate-based oxidation involving electron transfer, hydrogen abstraction, and radical addition can yield by-products whose polarity, persistence, and biological effects differ from those of the precursors [6–8]. Oxygenated organosulfur compounds,

including organosulfates, sulfonates, and other sulfur-containing oxidation products, can be produced by sulfate incorporation and oxidation of pre-existing organic sulfur. During sulfate incorporation, the addition of sulfate radicals to organic substrates can lead to organosulfates containing C-O-S linkages. In a study of sulfate radical-mediated oxidation involving 23 aromatic and five aliphatic model compounds, 25 substrates formed at least one stable sulfate-containing product, including phenyl sulfate and p-cresyl sulfate [9]. The formation of organosulfates has also been reported during UV/PDS treatment of natural organic matter (NOM), and seven target compounds were quantified at concentrations up to 203 ng/L [10]. In contrast, sulfur oxidation transforms a sulfur functionality already present in an organic precursor. Dimethyl sulfoxide and phenyl methyl sulfoxide were converted to their corresponding sulfones in Fe(II)/PMS and Fe(II)/PDS systems [11]. These pathways provide the chemical context for considering the occurrence, persistence, and potential biological effects of oxygenated organosulfur compounds. Oxygenated organosulfur compounds have been identified in tap water from eight European cities, with estimated total concentrations as high as 50 ng/L for haloacetonitrilesulfonic acids and 800 ng/L for haloacetaldehydesulfonic acids [12]. Low-concentration effects have been reported for bisphenol S, a related sulfone-containing compound, while tissue accumulation of indoxyl sulfate has been observed in animal experiments [13,14]. The co-occurrence of diverse organosulfur compounds and evidence of additive mixture effects raise potential toxicological concerns [10,12,15]. Bioassays of PMS-treated wastewater extracts also show that oxidation does not necessarily eliminate mixture toxicity [16]. Thus, the persulfate-based oxidation cannot be assumed to render treated water harmless, and attention should also be paid to the subsequent control of oxygenated organosulfur compounds.

Research on the subsequent removal of oxygenated organosulfur compounds has lagged significantly behind research on their formation and detection. Potential treatment options include further oxidation, membrane filtration, and adsorption. Reoxidation may generate new oxygenated organosulfur compounds with higher oxygen contents or smaller molecular sizes as the parent compounds are transformed [17]. Precise membrane rejection depends on molecular and membrane properties and must be balanced against water permeability [18,19]. Adsorption offers an alternative route through interactions such as electrostatic attraction and hydrogen bonding [20,21]. Previous studies have demonstrated adsorption of representative oxygenated organosulfur compounds using Zr-based metal–organic frameworks, MIL-100(Fe), and poly-β-cyclodextrin [21–23]. Molecular dynamics and fluid-assisted analyses have also been used to investigate the adsorption behavior of these adsorbents [24,25]. These findings provide a basis for investigating the adsorption of oxygenated organosulfur compounds. However, the adsorptive removal of oxygenated organosulfur compounds from persulfate-treated waters and the persistence of these compounds in adsorption effluents remain insufficiently characterized, particularly in complex water matrices.

In this study, micron-sized amorphous ZrO_x (MA-ZrO_x) was evaluated as a hydroxyl-bearing adsorbent for the capture of oxygenated organosulfur compounds remaining after PMS oxidation. The micron-sized form was selected for its potential to facilitate gravity-assisted solid–liquid separation and subsequent adsorbent recovery. This study also examined whether interactions identified for representative oxygenated organosulfur compounds corresponded to formula-level capture patterns in complex waters. Following synthesis and characterization, adsorption experiments using MA-ZrO_x were conducted at trace concentrations with seven representative compounds previously reported in the literature [10]. Density functional theory (DFT) calculations were employed to examine compound-specific removal, multiple hydrogen-bonding contacts, and steric accessibility. The sequential treatment process comprising PMS oxidation followed by MA-ZrO_x ad-

sorption was then investigated in NOM-simulated water, Yiwu Lake water, and Shanghai Reservoir water using total organic carbon (TOC) measurements and Fourier transform ion cyclotron resonance mass spectrometry (FT-ICR MS) data analysis. The formula-level analysis distinguished oxidation-emergent from pre-existing candidates and examined associations between apparent capture and nominal carbon oxidation state, unsaturation, O/N composition, and CH_2 increments. The specific contribution of this study is the evaluation of a micron-sized amorphous oxide for post-PMS adsorption by linking adsorption performance, modeled interfacial interactions, and compositional capture patterns. Together, these analyses assess the potential of MA-ZrO_x for the downstream control of oxygenated organosulfur compounds in persulfate oxidation effluents.

2. Materials and Methods

2.1. Chemical Reagents and Water Samples

Zirconium tetrachloride, ethanol, urea, methanol, formic acid, and hydrochloric acid were obtained from Aladdin (Shanghai, China). 1H-Indol-3-yl potassium sulfate (1H-Indol PS), potassium 4-methylumbelliferyl sulfate (4-MeS), 4-ethylbenzenesulfonic acid (4-Et BSA), potassium 2,5-dihydroxybenzenesulfonate (2,5-diOH BS), potassium 4-hydroxyphenyl sulfate (4-OH PS), sodium 3-carboxybenzenesulfonate (3-COOH BSA), and 2-methylbenzenesulfonic acid (2-Me BSA) were supplied by Macklin (Shanghai, China) NOM was purchased from Sigma-Aldrich (St. Louis, MO, USA). Ultrapure water (18.2 MΩ·cm) was produced using a Milli-Q system (Sigma-Aldrich). All chemicals listed above were used as received without additional purification.

NOM-simulated water was prepared by dissolving NOM in ultrapure water to obtain a carbon concentration of 6.4 mg C/L. No additional inorganic salts were added. Natural water samples were collected from two sites in China: a lake in Yiwu (Zhejiang Province) and a reservoir in Shanghai. Before the experiments, all samples were filtered through 0.45 μm glass-fiber filters and stored at 4 °C in the dark until use. The key physicochemical properties of the natural water samples are summarized in Table 1.

Table 1. Physicochemical properties of the natural water samples.

Parameter	Yiwu Lake	Shanghai Reservoir
pH	7.6	7.4
DOC [1] (mg/L)	1.34	2.78
Turbidity (NTU)	3.22	2.91
Cl^- (mg/L)	7.38	21.76
SO_4^{2-} (mg/L)	3.94	35.53
NO_3^- (mg/L)	0.54	1.47
F^- (mg/L)	1.92	0.20
Na (mg/L)	8.63	17.36
K (mg/L)	1.61	2.66
Ca (mg/L)	3.49	35.6
Mg (mg/L)	0.71	7.96
Fe (mg/L)	0.006	0.002
Mn (mg/L)	ND [2]	ND
Al (mg/L)	0.004	0.006
Sr (mg/L)	0.021	0.195

[1] DOC denotes dissolved organic carbon measured after filtration through 0.45 μm glass fiber filters. [2] ND, not detected.

2.2. Preparation and Characterization of Micron-Sized Amorphous ZrO_x

The adsorbent was synthesized as follows: 1.33 mmol of $ZrCl_4$ was dissolved in 50 mL of ethanol, while urea (0.1 mol) was dissolved in a mixture of 14 mL of water and 86 mL of

ethanol. After complete dissolution, the two solutions were mixed thoroughly. The mixed solution was transferred into a Teflon-lined autoclave and heated at 200 °C for 15 h. The obtained precipitate was collected, washed with water and ethanol, and dried overnight at 60 °C. Surface morphology was examined using a field-emission scanning electron microscope (SU8010, Hitachi, Tokyo, Japan). The particle-size distribution was measured using a Zetasizer Nano ZS analyzer (Malvern Instruments, Malvern, UK). Transmission electron microscopy (TEM), high-resolution transmission electron microscopy (HRTEM), selected-area electron diffraction (SAED), and scanning transmission electron microscopy (STEM) analyses were performed using a Talos F200X microscope (Thermo Fisher Scientific, Waltham, MA, USA) operated at an accelerating voltage of 200 kV. High-angle annular dark-field (HAADF) imaging was employed in STEM mode, and energy-dispersive X-ray spectroscopy elemental mapping was used to determine the spatial distributions of elements. X-ray diffraction (XRD) patterns were collected using an Empyrean diffractometer (PANalytical, Almelo, the Netherlands), and Fourier transform infrared (FTIR) spectra were recorded on a Frontier spectrometer (PerkinElmer, Shelton, CT, USA).

The gravity-settling behavior of the adsorbent was examined in a measuring cylinder at a dose of 1 g/L. The time at which stirring ceased was defined as t = 0. Digital photographs were acquired at 0, 2, 5, 8, 15, and 25 min to document the settling process. An additional gravity-settling experiment was conducted over 50 min using an MA-ZrO_x suspension at 1 g/L with an initial suspension height of 23 cm. The supernatant-layer height and supernatant turbidity were monitored over time. For the H-D exchange experiments, the material was loaded into a cell, and D_2 was introduced. The sample was heated from 40 to 700 °C at a nominal heating rate of 10 °C/min. Gas-phase products were monitored using an INFICON RGA MPH 100 residual gas mass spectrometer operated at 70 eV with an emission current of 2000 μA. Signals at m/z = 3 and 4 were recorded at 2 °C intervals during heating. The m/z = 3 signal was used to monitor HD formation, and m/z = 4 was used as the D_2 reference signal.

2.3. Adsorption Performance Evaluation

Batch adsorption experiments were conducted with the seven representative oxygenated organosulfur compounds. Each compound was tested separately at an initial concentration of 100 ng/L. The adsorbent (1 g/L) was introduced into 20 mL of the tested solution under continuous agitation. After a contact time of 10 min, samples were collected to determine the residual concentrations. The adsorbent was regenerated using a 0.1% NaOH solution, and its reusability was evaluated by measuring the removal efficiencies of two selected compounds (4-MeS and 4-Et BSA). Sequential oxidation–adsorption experiments were performed using three water matrices: NOM-simulated water, Yiwu Lake water, and Shanghai Reservoir water. For each water matrix, raw water was treated with PMS at a dosage of 0.10 g/L using a Co_2MnO_4-loaded microporous ceramic membrane. Co_2MnO_4 was coated on the inner walls of the membrane pores throughout the ceramic membrane, with a total loading of 0.7 g. The catalytic membrane had an approximate pore size of 1 μm and a thickness of about 0.55 cm. Oxidation was conducted at 20 ± 2 °C and without pH adjustment. The permeate flow rate was maintained at approximately 10 mL/min. The resulting oxidation effluent was stored under refrigeration in the dark until use. This oxidation effluent was then used as the influent for MA-ZrO_x adsorption, which was conducted at an adsorbent dosage of 1 g/L for 20 min at 20 °C under continuous stirring. Samples were collected for further analyses at three stages: before PMS oxidation, after PMS oxidation, and after subsequent MA-ZrO_x adsorption.

2.4. Water Quality Analysis and Quantification of Oxygenated Organosulfur Compounds

Organic carbon concentrations were determined using a multi-N/C 3100 TOC analyzer (Analytik Jena GmbH+Co. KG, Jena, Germany). Turbidity was measured with a 2100 Q portable turbidimeter (Hach, Loveland, CO, USA). The concentrations of Cl^-, SO_4^{2-}, NO_3^-, and F^- were quantified by ion chromatography using a Dionex Integrion HPIC system (Thermo Fisher Scientific, Waltham, MA, USA). The concentrations of Na, K, Ca, Mg, Fe, Mn, and Al were determined using inductively coupled plasma optical emission spectrometry (ICP-OES).

The seven representative compounds were quantified using an Agilent 1260 liquid chromatography (Agilent Technologies, Waldbronn, Germany) system coupled to an AB SCIEX 5600 quadrupole time-of-flight mass spectrometer (AB SCIEX, Concord, ON, Canada). Separation was performed on an ACQUITY UPLC BEH C_{18} Column (Waters Corporation, Milford, MA, USA). The mobile phases were composed of 0.1% formic acid in water (phase A) and methanol (phase B), and the separation was carried out at a column temperature of 35 °C with a flow rate of 200 μL/min. The gradient program was as follows: 0.0–3.0 min 10% A, 3.0–9.0 min 10–95% A, 9.0–30.0 min 95% A, 30.0–35.5 min 10% A. The mass spectrometer was operated in multiple reaction monitoring (MRM) mode and negative mode, with detailed instrument parameters listed in Table 2. Quantification was based on compound-specific calibration curves established using standards at 5, 10, 25, 50, and 100 ng/L. The coefficients of determination (R^2) ranged from 0.993 to 0.999. The calibration curves and their corresponding R^2 values are provided in Figure A1.

Table 2. The detection conditions for the seven representative oxygenated organosulfur compounds.

Compound	RT (min)	Q1 (*m*/*z*)	Q3 (*m*/*z*)	DP (V)	CE (eV)
1H-Indol PS	14.8	211.8	132	−28	−25
4-MeS	18.6	255	176	−60	−28
4-Et BSA	22.3	185.3	170.7	−96	−31
2,5-diOH BS	8.2	188.3	109.1	−20	−30
4-OH PS	9.9	172.5	108	−95	−30
3-COOH BSA	11.5	200.5	158	−35	−20
2-Me BSA	14.5	170.6	80.2	−50	−39

2.5. DFT Calculations of Organosulfur Adsorption Complexes

A finite cluster containing 12 Zr, 48 O, and 14 H atoms ($Zr_{12}O_{48}H_{14}$) was used as the host model [26,27]. The bare host was assigned a total charge of 0 and a spin multiplicity of 1 and contained 14 hydroxyl groups. A series of initial adsorption configurations was generated for the representative oxygenated organosulfur compounds, with the cluster hydroxyl groups serving as candidate adsorption sites. All DFT calculations were performed using Gaussian software [28]. Geometry optimizations were carried out using the PBE0 hybrid density functional, combined with Grimme's D3 correction and Becke–Johnson damping [29–31]. The 6-311G(d,p) basis set was employed for H, C, N, O, and S atoms, whereas Zr was represented by the Stuttgart/Dresden SDD effective core potential and its associated valence basis set [32–34]. Solvent effects were incorporated using the SMD continuum solvation model [35]. An ultrafine numerical integration grid was used. Self-consistent-field convergence was assisted by the XQC procedure. The adsorption energy was calculated using Equation (1):

$$E_{ads}^{sol} = E_{complex}^{sol} - E_{host}^{sol} - E_{adsorbate}^{sol}, \quad (1)$$

where $E_{complex}^{sol}$, E_{host}^{sol}, and $E_{adsorbate}^{sol}$ denote the total energies of the optimized complex, isolated host cluster, and isolated adsorbate, respectively. The discussion focused on

converged configurations selected in part for consistency between the calculated adsorption-energy trends and the experimental removal efficiencies.

2.6. Organic Matter Extraction, FT-ICR MS Analysis, and Formula-Level Data Processing

Organic matter was extracted from raw water, PMS oxidation effluent, and subsequent MA-ZrO_x adsorption effluent by solid-phase extraction (SPE; GL Sciences, Tokyo, Japan). For each sample, 1000 mL was acidified to pH 2 with hydrochloric acid. The pending samples were then passed through Bond Elut PPL cartridges that had been sequentially conditioned with methanol and Milli-Q water (pH = 2). The loading flow rate was 5 mL/min. After extraction, the retained NOM was eluted with 10.0 mL of methanol, and the eluate was concentrated to 0.5 mL under a gentle stream of N_2 and stored in the dark until further analysis. The extracts were characterized using FT-ICR MS (SolariX, Bruker, Bremen, Germany), and electrospray ionization (ESI) was operated in negative-ion mode. Samples were infused at a flow rate of 120 µL/h, with the capillary voltage set to −4.0 kV and the ion accumulation time set to 0.1 s. Mass spectra were acquired over an m/z range of 100–1600.

To better visualize changes in organic matter with different chemical characteristics during oxidation and adsorption, the molecular formulas were plotted on van Krevelen diagrams. The H/C and O/C atomic ratios for each molecular formula were calculated separately. The assigned oxygenated organosulfur formulas were classified into two categories: CHOS (N = 0, S $\geq$ 1) and CHONS (N $\geq$ 1, S $\geq$ 1). Based on their elemental stoichiometry, assigned formulas were divided into seven regions: lipids, aliphatic/proteins, lignins/CRAM-like structures, carbohydrates, unsaturated hydrocarbons, aromatic structures, and tannins [36].

For molecular-level capture analysis, formulas with S = 1 and O $\geq$ 4 were selected from the FT-ICR MS data as oxygenated organosulfur candidates [37,38]. Candidates detected in the oxidation effluent but not in the adsorption effluent were classified as apparently captured, and those detected in both oxidation effluent and adsorption effluent were classified as persistent. The apparent capture proportion was calculated using Equation (2):

$$p_{capture} = n_{capture}/(n_{capture} + n_{persistent}) \times 100\%. \quad (2)$$

Two-sided 95% confidence intervals were calculated using the Wilson score method [39]. The molecular descriptors examined were $\log_{10}$-transformed signal intensity in the oxidation effluent, m/z, O-atom count, O/C, H/C, nominal oxidation state of carbon (NOSC), (DBE-O)/C, and AI_{mod} [40,41]. Descriptor differences between apparently captured and persistent candidates were summarized by Cliff's δ [42].

The paired odds ratio (OR) was calculated using Equation (3):

$$OR_{pair} = b/c, \quad (3)$$

where b denotes the number of pairs in which only the increment-bearing member was apparently captured, and c denotes the number of pairs in which only the reference member was apparently captured.

3. Results

3.1. Structure and Surface Chemistry of Micron-Sized Amorphous ZrO_x

The particle size and sedimentation behavior of MA-ZrO_x are shown in Figure 1. The SEM image illustrates predominantly micron-sized particles, with the measured particle-size distribution concentrated at approximately 1.5–2.5 µm (Figure 1a). The higher-magnification SEM image provides a clearer view of the nearly spherical contour of an individual MA-ZrO_x particle (Figure 1b).

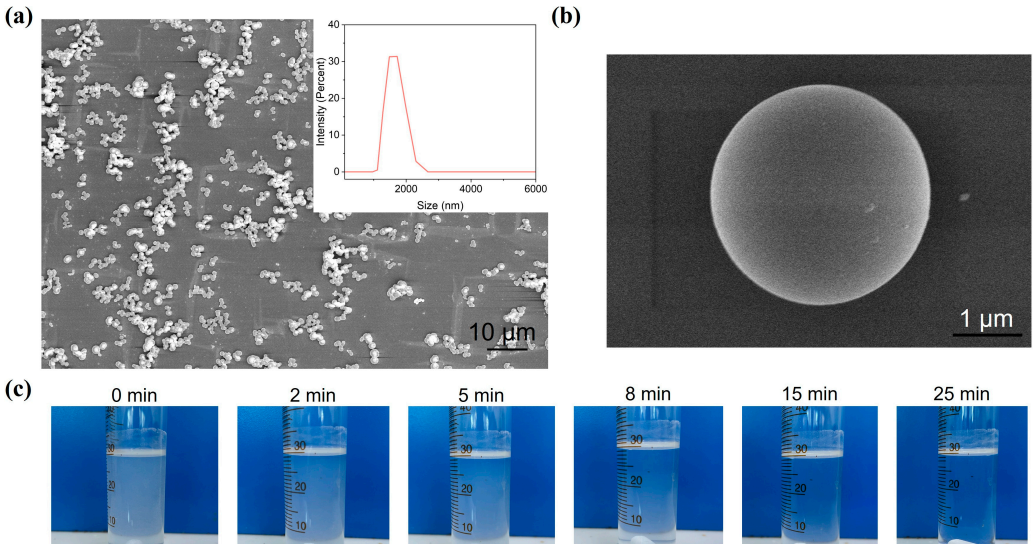


Figure 1. (**a**) SEM image of MA-ZrO_x with the particle-size distribution shown in the inset; (**b**) higher-magnification SEM image of an individual MA-ZrO_x particle; and (**c**) sedimentation behavior of MA-ZrO_x (1 g/L) after 0, 2, 5, 8, 15, and 25 min.

After adsorption, MA-ZrO_x exhibited favorable solid–liquid separation performance (Figure 1c). Significant sedimentation was observed after 2 min of standing, and a distinct interface between the clarified supernatant and the underlying suspension became visible after 5 min. As sedimentation progressed, the interface gradually moved downward. By 25 min, the liquid phase had become markedly clearer. To complement these observations, an additional settling experiment was conducted over 50 min (Figure A2). The supernatant-layer height increased with settling time, while the supernatant turbidity decreased. For an initial suspension height of 23 cm, the supernatant-layer height reached approximately 7.5 cm after 50 min, and the supernatant turbidity was approximately 61.5 NTU. In contrast, gravity-driven clarification can be challenging for dispersions of nanoscale adsorbents [43]. As the estimated sedimentation time is inversely proportional to the square of the particle radius, the micron-sized particle size contributed to the favorable gravity-driven separation performance of MA-ZrO_x [44]. Considering that nanoscale dimensions can facilitate cellular uptake and transport across biological barriers, this separation behavior may help mitigate the risks associated with nanoscale adsorbents in water treatment [45–47].

The structure of MA-ZrO_x was characterized by TEM (Figure 2). The low-magnification TEM image revealed the nearly spherical particle morphology of MA-ZrO_x particles (Figure 2a). As shown in Figure 2b,c, no clear and continuous lattice fringes were observed in the HRTEM image, and the corresponding SAED pattern exhibited a diffuse halo. In addition, the XRD pattern was dominated by broad peaks without discernible sharp diffraction peaks (Figure A3). These observations support the predominantly amorphous nature of MA-ZrO_x. The HAADF-STEM image and elemental maps showed homogeneous distributions of Zr and O within the particle (Figure 2d–f).

The surface chemistry of MA-ZrO_x was further examined using FTIR spectroscopy and H-D isotope exchange (Figure 3). As shown in Figure 3a, the broad absorption band at 3600–2500 cm^{-1} and the band near 1560 cm^{-1} are attributed to O-H stretching vibrations of residual water and water-perturbed -OH [48,49]. The absorption near 1154 cm^{-1} can be assigned to surface -OH on MA-ZrO_x [50]. H-D exchange was subsequently used to quantify the active surface -OH (Figure 3b) [51]. To minimize contributions from variations in D_2 concentration, the HD response was normalized against the D_2 signal. The HD/D_2 experimental profile was deconvoluted, resulting in a sharp peak at approximately 285 °C and a broad shoulder at 375 °C. This suggested that exchangeable hydrogen was associated

with surface -OH in two distinct chemical environments. The lower-temperature component is potentially assigned to less coordinated Zr-OH environments, while the broader high-temperature component may arise from multiply coordinated hydroxyls, including bridging Zr-OH-Zr structures [51,52]. These results support the presence of exchange-active surface -OH, which may contribute to the adsorption of sulfur-containing species [53,54].

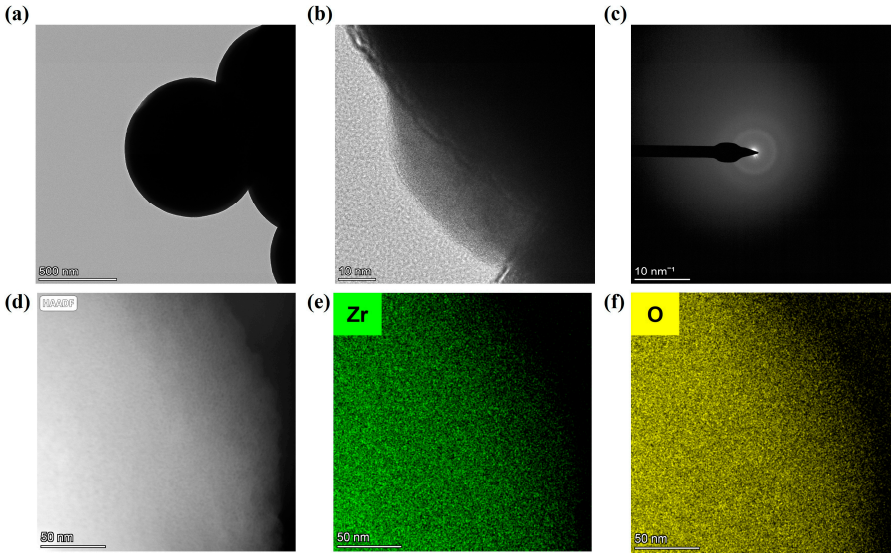


Figure 2. (**a**) Low-magnification TEM image, (**b**) HRTEM image and (**c**) corresponding SAED pattern, and (**d**) HAADF-STEM image and corresponding elemental mappings of (**e**) Zr and (**f**) O.

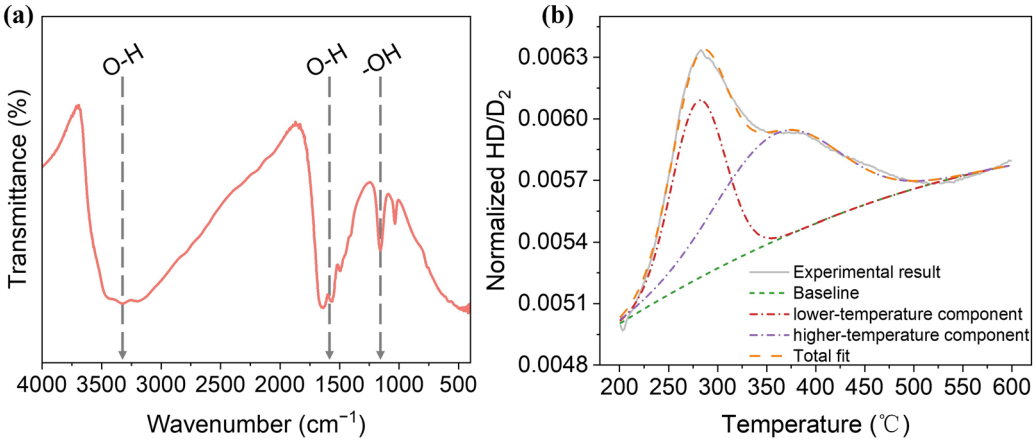


Figure 3. (**a**) FTIR spectrum and (**b**) H-D exchange of MA-ZrO_x.

3.2. Removal Efficiency of Representative Oxygenated Organosulfur Compounds

To initially evaluate the adsorption performance of MA-ZrO_x toward oxygenated organosulfur compounds, seven representative compounds identified during sulfate radical-mediated oxidation in NOM-containing water were used: 1H-Indol PS, 4-MeS, 4-Et BSA, 2,5-diOH BS, 4-OH PS, 3-COOH BSA, and 2-Me BSA (Figure 4). At an initial concentration of 100 ng/L, removal efficiencies differed among the compounds, with five reaching at least 98% removal (Figure 4a). The removal efficiencies of 4-MeS, 1H-Indol PS, and 4-OH PS were 100.0%, 100.0%, and 99.8%, respectively, while those of 2,5-diOH BS and 3-COOH BSA were 98.2% and 98.0%. Lower removal was observed for 4-Et BSA (88.9%) and 2-Me BSA (60.1%). Furthermore, 4-MeS and 4-Et BSA were selected to evaluate the reusability of MA-ZrO_x over five adsorption–regeneration cycles (Figure 4b). The removal efficiencies of both compounds decreased slightly over the five cycles, supporting the cycling stability of MA-ZrO_x for the capture of oxygenated organosulfur compounds.

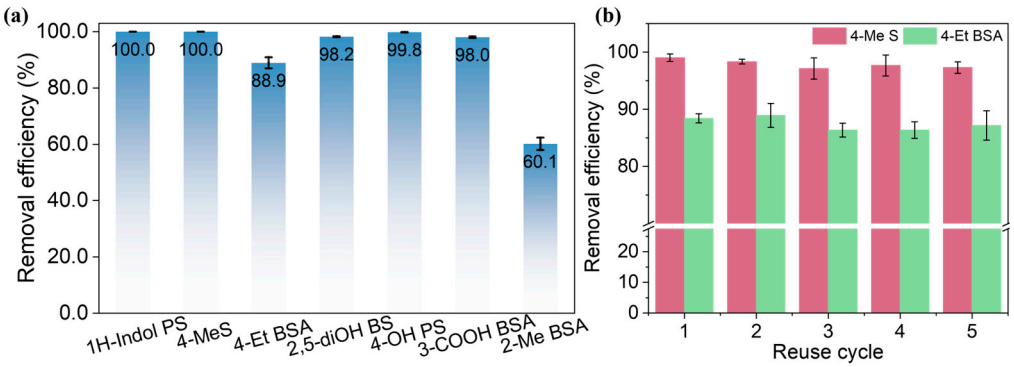


Figure 4. (**a**) Removal efficiencies and (**b**) reusability of MA-ZrO_x for oxygenated organosulfur compounds.

3.3. Adsorption Analyses of Representative Oxygenated Organosulfur Compounds

Differences in removal efficiency suggest that molecular structural features beyond the sulfate ester or sulfonate groups may also influence adsorption by MA-ZrO_x. To probe the molecular basis of this selectivity, adsorption complexes on MA-ZrO_x were constructed and optimized (Figure 5). Among the seven compounds, 4-MeS exhibits the most negative adsorption energy (−28.0 kcal/mol). In its optimized configuration, two spatially separated O atoms accept hydrogen bonds from two surface -OH groups, with contact distances of 1.94 and 1.99 Å, respectively. A different binding motif is observed for 4-OH PS, with an adsorption energy of −26.2 kcal/mol. A surface -OH donates a hydrogen bond to an O atom of the sulfate group at a distance of 1.93 Å, whereas the phenolic hydroxyl in 4-OH PS donates a hydrogen bond to a surface O site at 1.77 Å. Similar binding motifs are observed for 1H-Indol PS and 2,5-diOH BS, with adsorption energies of −25.1 and −24.9 kcal/mol, respectively. For 1H-Indol PS, an O atom of the sulfate group accepts a hydrogen bond from a surface -OH at 1.98 Å, while the N-H group donates a hydrogen bond to a surface O atom at 1.76 Å. In the optimized configuration of 2,5-diOH BS, one anchoring interaction involves a surface -OH and an O atom of the sulfur-containing group, whereas the second is provided by the phenolic hydroxyl group interacting with the surface. 3-COOH BSA has an adsorption energy of −21.9 kcal/mol. In its optimized structure, one surface -OH group interacts with an oxygen atom of the sulfur-containing group, with an O···H distance of 1.83 Å, while a second -OH interacts with a carboxyl oxygen at 2.10 Å. The optimized configurations of 4-Et BSA and 2-Me BSA each feature one principal hydrogen-bonding contact, but their adsorption energies differ considerably. For 4-Et BSA, a surface -OH interacts with an oxygen atom of the sulfur-containing group at 1.84 Å, corresponding to an adsorption energy of −19.8 kcal/mol. In contrast, 2-Me BSA has the least negative adsorption energy (−11.1 kcal/mol), despite a relatively short -OH···O contact of 1.87 Å. The ortho-methyl substituent may impose steric constraints near the sulfur-containing group, thereby limiting favorable contact between the molecule and the MA-ZrO_x surface [55,56]. Overall, the negative adsorption energies indicate that the adsorption is energetically favorable for all seven representative compounds. The calculated adsorption energies of the selected configurations were compared with the experimentally measured removal efficiencies (Figure A4). Because agreement with experimental results contributed to configuration selection, this comparison is exploratory, and it serves to generate hypotheses for the subsequent formula-level analysis of apparent capture in complex waters. These observations suggest that additional functional groups, such as phenolic -OH, N-H, or carboxyl groups, can provide secondary surface contacts, potentially enhancing adsorption. Meanwhile, steric restriction near the primary binding group could limit favorable accommodation of the molecule on the MA-ZrO_x surface.

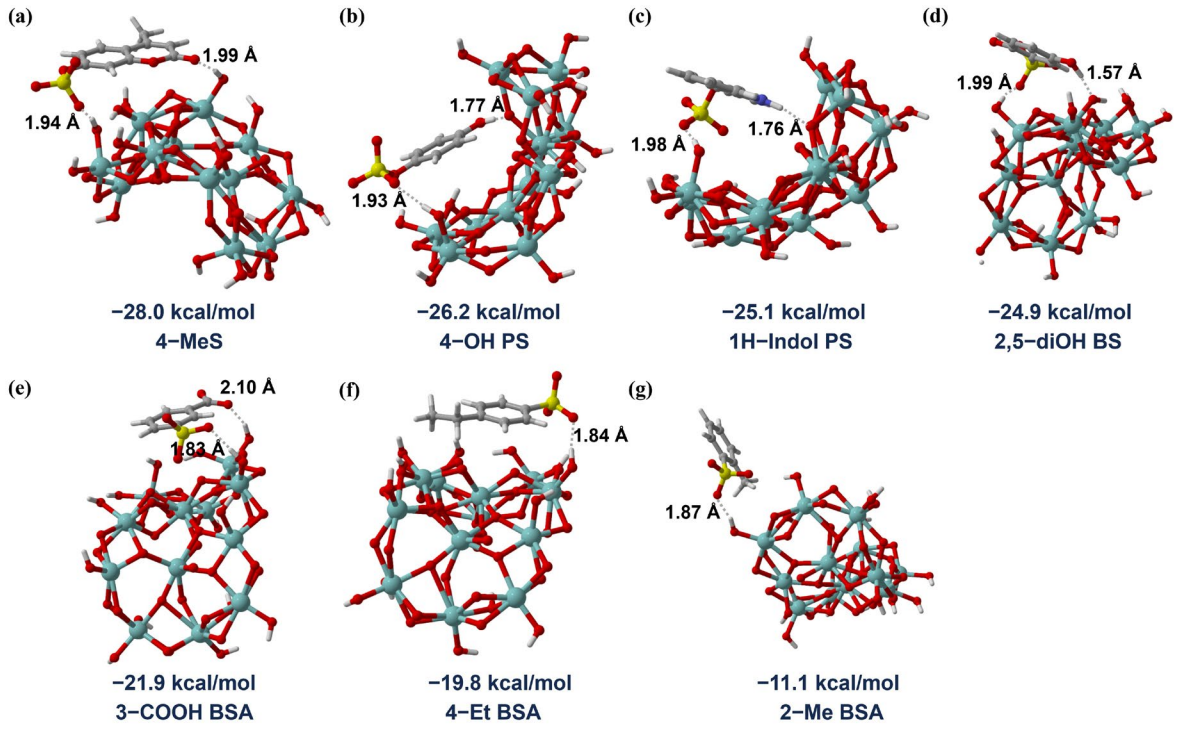


Figure 5. DFT-optimized adsorption configurations of seven representative oxygenated organosulfur compounds on MA-ZrO_x: (**a**) 4–MeS, (**b**) 4–OH PS, (**c**) 1H–Indol PS, (**d**) 2,5–diOH BS, (**e**) 3–COOH BSA, (**f**) 4–Et BSA, (**g**) 2–Me BSA.

3.4. Applicability of Micron-Sized Amorphous ZrO_x Adsorption to Complex Water Matrices

To evaluate the applicability of MA-ZrO_x as a post-oxidation adsorbent, NOM-simulated water, Yiwu Lake water, and Shanghai Reservoir water were subjected to sequential PMS oxidation and MA-ZrO_x adsorption. Figure 6a presents the TOC concentrations in raw water, PMS oxidation effluent, and the final effluent after the subsequent adsorption step. Compared with the corresponding PMS oxidation effluents, the final effluents showed a further 37.8–54.3% decrease in TOC, demonstrating additional organic-carbon removal. FT-ICR MS was used to investigate the changes in the number of detected oxygenated organosulfur compounds (Figure 6b). Following MA-ZrO_x adsorption, the total number of detected oxygenated organosulfur formulas and the number of CHOS and CHONS formulas consistently decreased in three water matrices, indicating the applicability of MA-ZrO_x in the actual PMS oxidation effluent remediation.

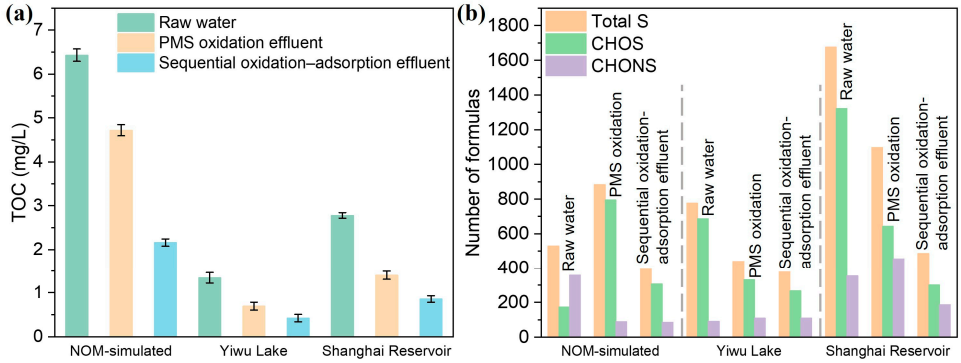


Figure 6. Changes in (**a**) TOC concentration and (**b**) the number of detected oxygenated organosulfur compounds at successive stages of PMS oxidation followed by MA-ZrO_x adsorption in three water matrices.

To identify which formulas were lost or whether the remaining compositions shifted, the van Krevelen diagrams were further employed among water matrices and treatment stages (Figure 7). Obviously, the MA-ZrO_x post-adsorption distributions largely overlapped those of the oxidation effluents in the H/C and O/C combined space, while the number of detected formulas declined within these occupied regions. It is worth noting that a considerable number of oxygenated organosulfur compounds were also detected in the two natural waters before PMS treatment (Figure A5). Some specific oxygenated organosulfur compounds have been identified as novel precursors, which could form disinfection by-products, including halogenated sulfonic acids [12,57]. Therefore, even without PMS treatment, introducing MA-ZrO_x adsorption into traditional water treatment may also reduce the formation of disinfection by-products by capturing oxygenated organosulfur compounds.

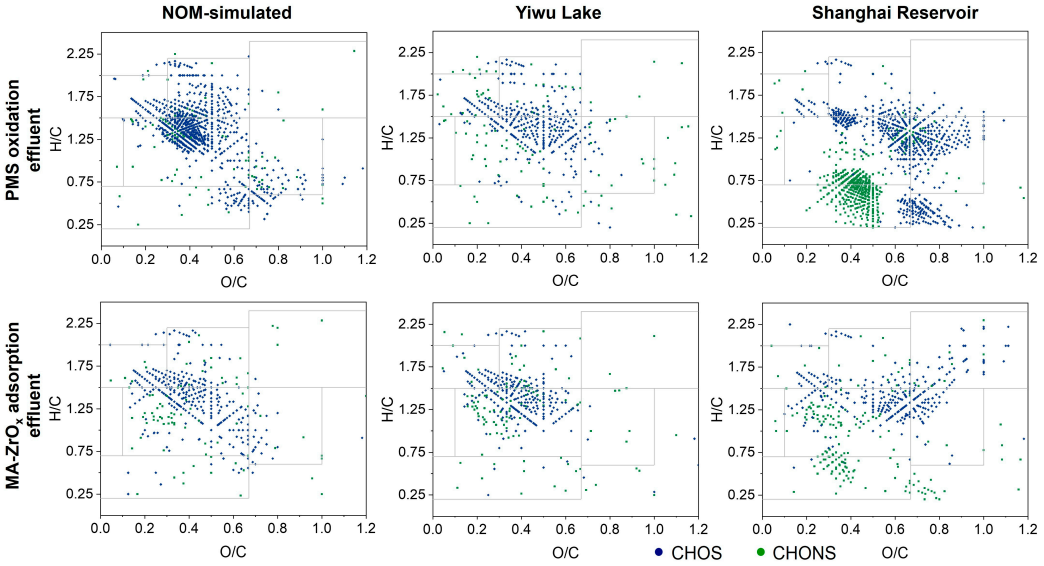


Figure 7. Van Krevelen distributions of CHOS and CHONS molecular formulas in the PMS oxidation effluents (**top row**) and the MA-ZrO_x adsorption effluents (**bottom row**) of three water matrices.

Furthermore, apparent capture was compared between pre-existing and oxidation-emergent candidate formulas during MA-ZrO_x adsorption (Figure A6). Within each matrix, formulas detected in both the raw water and the oxidation effluent were classified as pre-existing, whereas those detected in the oxidation effluent but not in the raw water were classified as oxidation-emergent. Among the three different water matrices, the apparent capture rate of the oxidation-emergent formulas is consistently higher than that of the pre-existing formulas: 75.3% versus 51.1% in NOM-simulated water, 78.5% versus 37.3% in Yiwu Lake water, and 91.6% versus 60.8% in Shanghai Reservoir water. The difference between them is more pronounced in the two natural waters.

3.5. Associations Between Molecular Composition and Apparent Capture

In order to further investigate the origin of the differences in the capture of various oxygenated organosulfur compounds, the associations between molecular composition and apparent capture were investigated. Generally, the higher capture rate can be found in parts of the positive-NOSC region, particularly where (DBE-O)/C was also positive (Figure A7a). Cliff's δ was then used to compare descriptor distributions between apparently captured and retained formulas within each water matrix (Figure A7b). As positive δ values indicate higher descriptor values in the captured group, it can be found that apparently captured formulas in the MA-ZrO_x adsorption generally have a higher nominal mass, more oxygen atoms, and a lower hydrogen saturation.

The descriptor analysis identifies broad associations but does not isolate particular elemental increments. In light of the additional O- and N-containing contacts suggested by the DFT models, differences in apparent capture among O/N-defined formula groups were further examined (Figure 8). Within the oxygenated organosulfur candidate set, formulas were assigned to four groups: O = 4, N = 0; O ≥ 5, N = 0; O = 4, N ≥ 1; and O ≥ 5, N ≥ 1. Among N-free formulas, the O ≥ 5 group had higher apparent capture rates than the O = 4 reference group in all three matrices: 71.7% versus 33.3% in NOM-simulated water, 49.0% versus 20.8% in Yiwu Lake water, and 74.7% versus 15.4% in Shanghai Reservoir water. The O = 4 and N ≥ 1 groups also had higher capture than the reference group, at 100%, 100%, and 33.3%, respectively, although the wide intervals limit the strength of this comparison. Pooling formula records within each group across the three waters gave apparent capture rates of 25.7%, 68.8%, 89.5%, and 90.7%, respectively, for the four groups listed above. Overall, the molecules with additional O atoms or N atoms exhibited enhanced MA-ZrO_x adsorption removal across different matrices. As suggested by the DFT configurations, these compositional associations are consistent with a possible contribution from additional hydrogen-bonding functionalities.

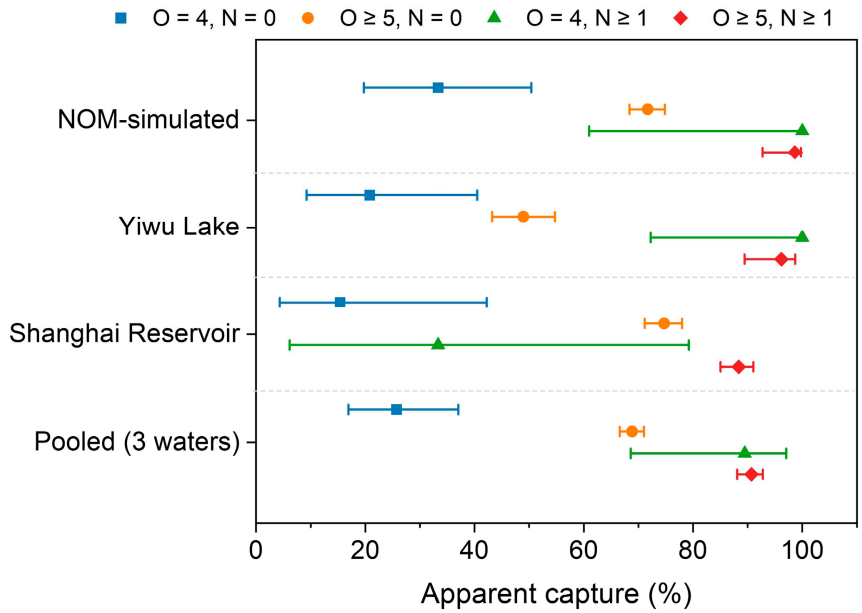


Figure 8. Apparent capture rates for O/N-defined groups within the oxygenated organosulfur compounds.

With heteroatom counts held constant, the association between CH_2 increments and apparent capture during MA-ZrO_x adsorption was further examined. Within each water matrix, exact formula pairs differed by k(CH_2), with C increasing by k and H by 2k while N, O, S and DBE remained unchanged (Figure 9). Comparisons were reported when at least 30 formula pairs were available. NOM-simulated water, Yiwu Lake water, and Shanghai Reservoir water met the criterion for k = 1–8, k = 1–2, and k = 1–6, respectively. In NOM-simulated water, the ORs were 0.57–0.71 for +1 to +3 CH_2 and 1.50–5.00 for +4 to +8 CH_2. In Yiwu Lake water, the ORs were 0.75 and 0.56 for +1 CH_2 and +2 CH_2, respectively. In Shanghai Reservoir water, the OR was 1.00 for +1 CH_2 and ranged from 0.48 to 0.68 for +2 to +6 CH_2. Apart from the relatively few comparisons in the Yiwu Lake group, both the NOM-simulated and Shanghai Reservoir groups exhibited a smaller CH_2 increment corresponding to a lower apparent capture, while the larger CH_2 increment showed a significant apparent capture recovery.

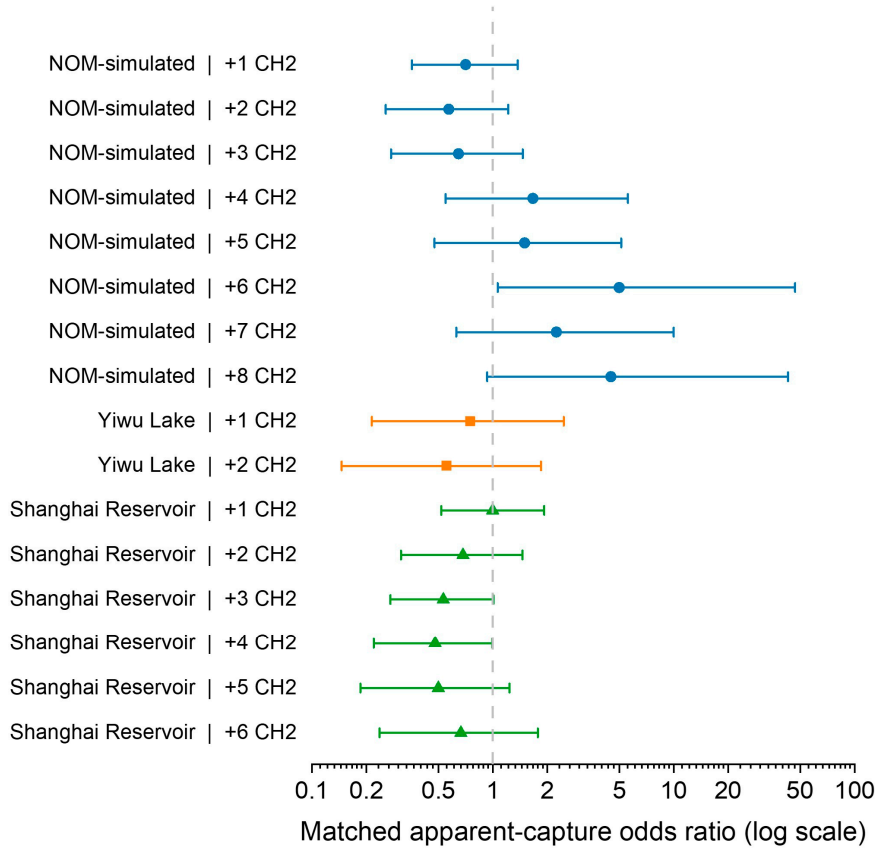


Figure 9. Paired odds ratios for apparent capture with k(CH_2) composition increments within the oxygenated organosulfur compound candidates.

4. Discussion

The adsorption experiments and DFT-optimized configurations suggest that multiple hydrogen-bonding contacts and steric accessibility contribute to the compound-dependent removal observed for the seven representative compounds. At the population level, the higher apparent capture of O-rich N-free formulas across the three matrices, together with the higher pooled capture of N-containing groups, is consistent with a possible contribution from additional polar contacts. Meanwhile, the compositional associations between the CH_2 increment and apparent capture might be due to the competition between local surface-contact constraints and stabilization associated with a larger nonpolar moiety. The 2-Me BSA DFT configuration discussed above motivates considering whether substitution near an anchoring group can restrict surface access or alter the geometry required for favorable polar contacts. At larger increments, an additional nonpolar moiety could partly compensate for an unfavorable local geometry through interactions with already adsorbed organic matter [58]. Structure-resolved homologues and quantitative adsorption measurements are further needed to test this proposed balance.

Together, the analyses extend the assessment from adsorption of individual compounds to the behavior of residual mixtures after PMS oxidation. The model-compound experiments and DFT calculations provide structure-specific information on removal and surface contacts, whereas FT-ICR MS characterizes apparent capture and persistence at the formula level. Their combined interpretation adds compositional information beyond TOC reduction.

Table A1 summarizes the reported performance of previously investigated adsorbents, NU-1000, MIL-100(Fe), and poly-β-cyclodextrin, alongside the results obtained for MA-ZrO_x. The present study complements these investigations by examining multiple

structurally distinct oxygenated organosulfur compounds and extending the evaluation to residual organic mixtures after PMS oxidation. Because adsorption uptake, individual-compound removal, and TOC reduction represent different performance metrics, and the target compounds and the background are different, the values in Table A1 do not establish a direct ranking of the adsorbents. Instead, the present results support the potential of MA-ZrO_x as a complementary post-PMS treatment material.

The observed gravity settling of MA-ZrO_x and maintained removal performance over five regeneration cycles support further evaluation of particle recovery and reuse. From a safety perspective, facilitating particle separation may help limit adsorbent carryover into the treated water and the associated potential exposure. However, these results do not establish greater chemical or mechanical stability than that of nanosized ZrO_x, which needs further research. Importantly, micrometer-sized adsorbents can be readily integrated with membrane filtration, enabling high-throughput treatment under relatively low driving pressures [59]. In this case, the adsorbent remains a discrete particulate phase that can be withdrawn for off-site regeneration or recirculation, while the membrane is retained in situ as the separation barrier. This process design could offer a practical balance among adsorption efficiency, particle recovery, and operational flexibility.

The management of spent regenerant should also be considered in assessing the practical application of MA-ZrO_x. Previous studies provide a basis for evaluating NaOH recovery and separate treatment of the organic-contaminant-containing residual stream [60,61]. This would address both regenerant consumption and the pollutants transferred during desorption.

5. Conclusions

Overall, MA-ZrO_x exhibited effective adsorption of oxygenated organosulfur compounds. Five of seven representative compounds reached at least 98% removal within 10 min at an initial concentration of 100 ng/L. DFT calculations associated more favorable adsorption with cooperative hydrogen-bonding contacts involving the sulfur-containing group and additional donor/acceptor sites, whereas single-site anchoring and steric constraints were associated with weaker binding. In NOM-simulated water and two natural waters (Yiwu Lake water and Shanghai Reservoir water), MA-ZrO_x adsorption following PMS oxidation removed 37.8–54.3% of residual TOC. Oxidation-emergent oxygenated organosulfur compounds consistently showed higher apparent capture than pre-existing compounds in all three matrices. The $O \geq 5$ group showed higher apparent capture than the $O = 4$ group among N-free candidates, and N-containing groups also showed higher pooled capture than the $O = 4$, $N = 0$ reference group. In the exact formula-pair comparisons, the CH_2 extension was associated with an initial decrease followed by a recovery in apparent capture, which might be due to the competition between local surface-contact constraints and stabilization associated with a larger nonpolar moiety. Together, the adsorption experiments, DFT calculations, and FT-ICR MS analysis support micron-sized amorphous ZrO_x as a candidate post-PMS adsorbent for the remediation of persulfate-treated effluent and provide complementary insight into compound-dependent removal and formula-level capture in complex waters.

Author Contributions: Conceptualization, J.X. and W.Q.; methodology, J.X. and W.Q.; software, J.Y.; validation, J.X. and W.Q.; formal analysis, J.X. and W.Q.; investigation, J.X. and W.Q.; resources, J.Y.; data curation, J.X. and W.Q.; writing—original draft preparation, J.X. and W.Q.; writing—review and editing, J.X. and W.Q.; visualization, J.X. and W.Q.; supervision, J.X. and W.Q.; project administration, J.X. and W.Q.; funding acquisition, W.Q. All authors have read and agreed to the published version of the manuscript.

Funding: This research was funded by the State Key Laboratory of Urban–Rural Water Resources and Environment (Harbin Institute of Technology), Grant No. 2025DX23.

Data Availability Statement: The original contributions presented in this study are included in the article. Further inquiries can be directed to the corresponding author.

Acknowledgments: We are grateful for resources from the High-Performance Computing Center of Central South University.

Conflicts of Interest: The authors declare no conflicts of interest.

Appendix A

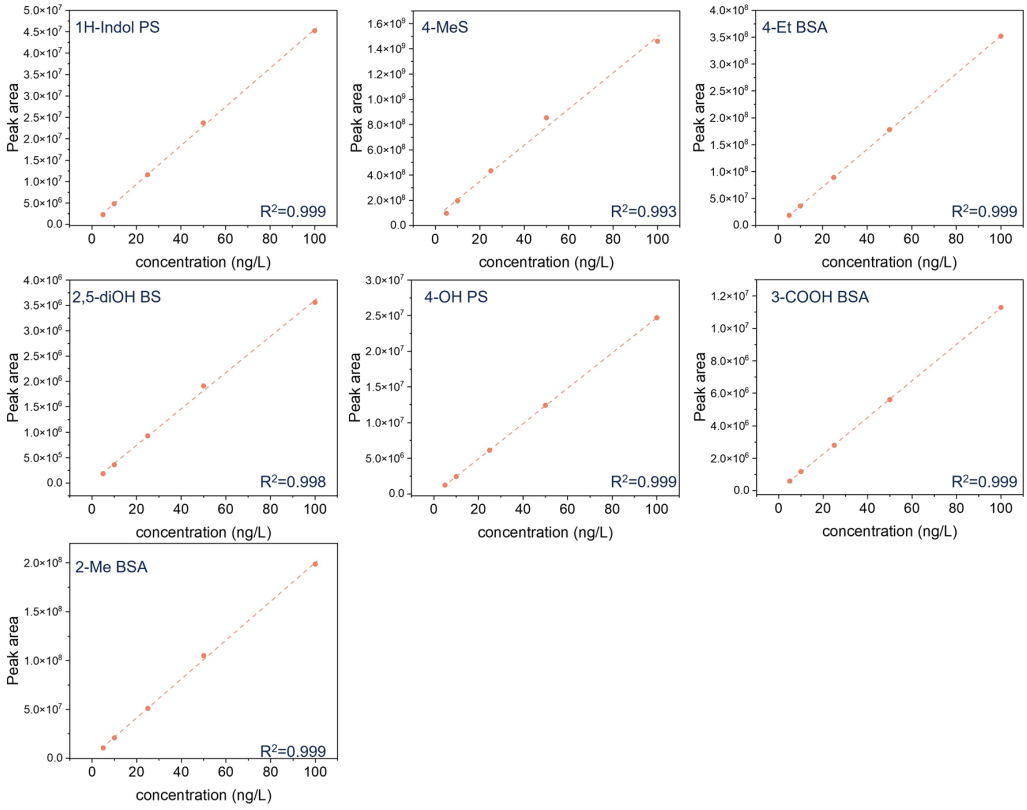


Figure A1. Calibration curves for the seven representative oxygenated organosulfur compounds.

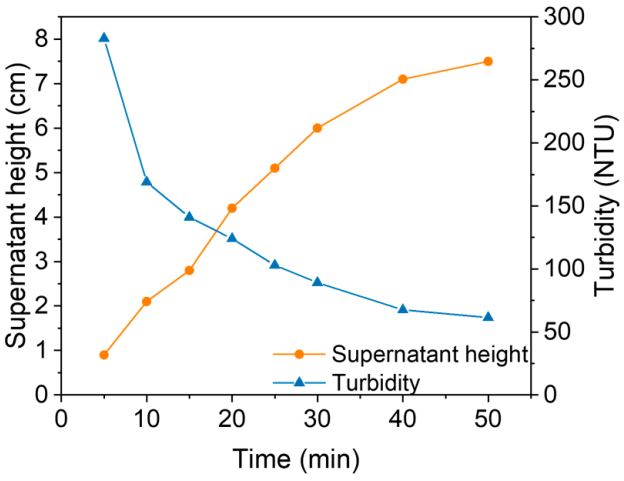


Figure A2. Time-dependent changes in supernatant-layer height and supernatant turbidity during gravity-settling.

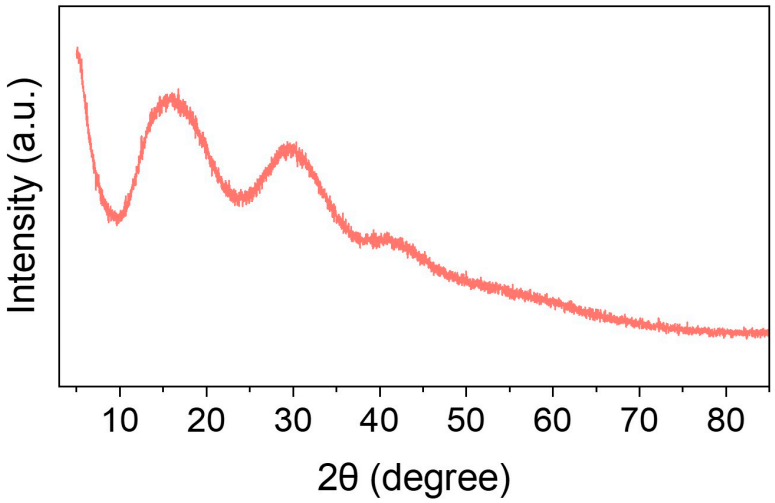


Figure A3. XRD pattern of the as-prepared MA-ZrO_x.

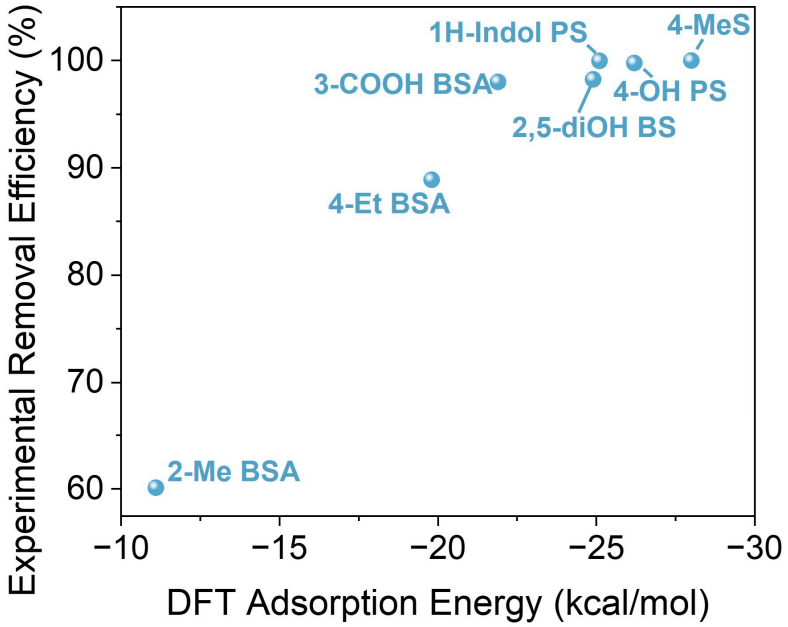


Figure A4. Comparison of DFT-calculated adsorption energies and experimentally measured removal efficiencies.

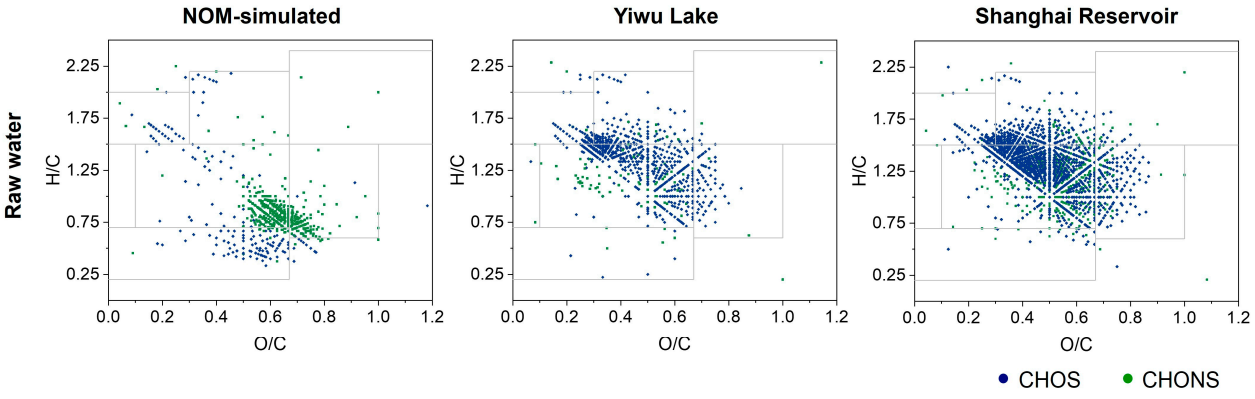


Figure A5. Van Krevelen distributions of CHOS and CHONS molecular formulas in three water matrices before PMS oxidation.

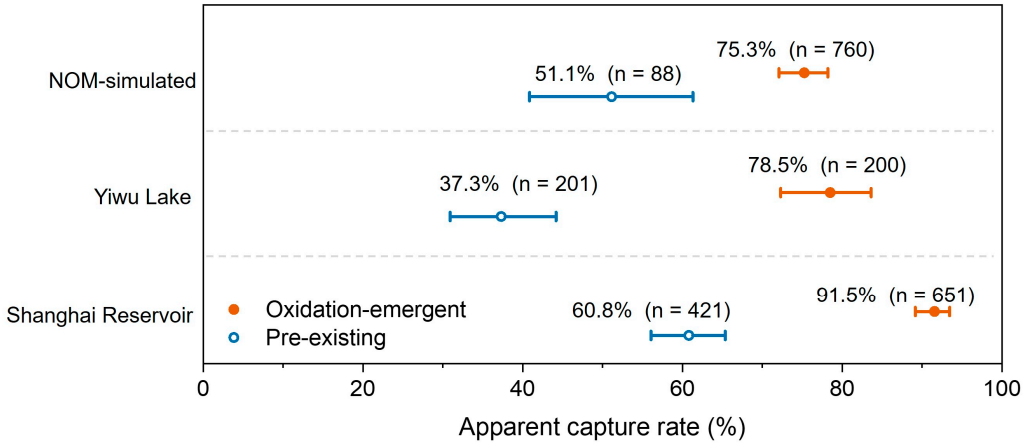


Figure A6. Apparent capture rates of oxidation-emergent and pre-existing oxygenated organosulfur formulas in three water matrices.

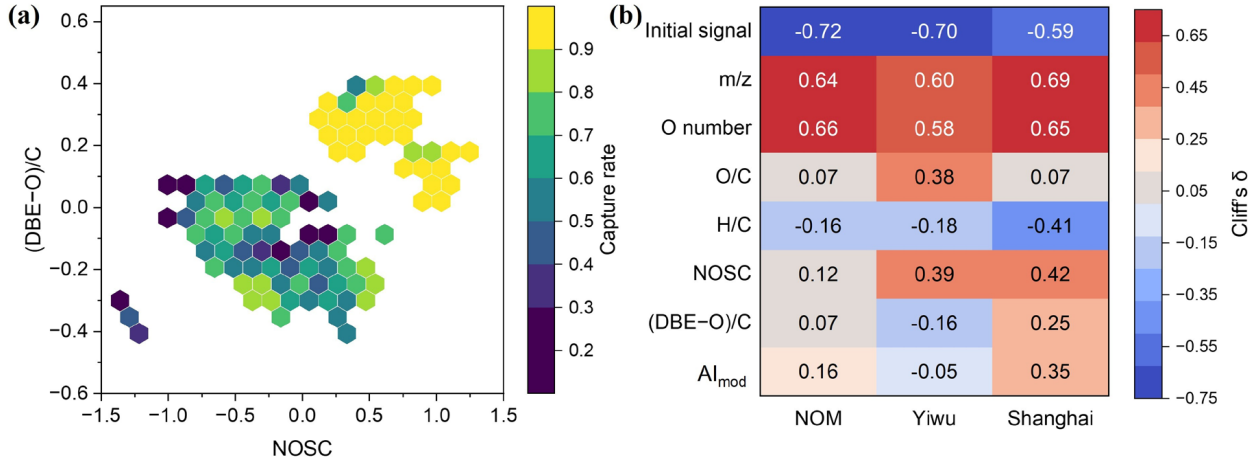


Figure A7. (**a**) Apparent capture rate in NOSC-(DBE-O)/C space; (**b**) Cliff's δ comparing initial signal and molecular descriptors between apparently captured and retained formulas within each water matrix.

Table A1. Comparison of adsorption performance reported in previous studies and the present work.

No.	Adsorbent	Target Compounds	Removal Result	Adsorption Uptake	Reference
1	NU-1000	indoxyl sulfate	98%	-	[21]
2	MIL-100(Fe)	p-Cresyl sulfate	-	68.6 nmol/mg	[22]
3	NU-1000	p-Cresyl sulfate	-	156.7 nmol/mg	[22]
4	Poly-β-cyclodextrin	p-Cresyl sulfate	-	263 mg/g	[23]
5	MA-ZrO_x	Seven representative compounds	60.1–100.0%	-	This study
6	MA-ZrO_x	PMS oxidation effluents of different water samples	37.8–54.3% further TOC reduction	-	This study

References

1. McGachy, L.; Sedlak, D.L. From Theory to Practice: Leveraging Chemical Principles To Improve the Performance of Peroxydisulfate-Based In Situ Chemical Oxidation of Organic Contaminants. *Environ. Sci. Technol.* **2023**, *58*, 17–32. [CrossRef] [PubMed]
2. Liang, C.; Yin, S.; Huang, P.; Yang, S.; Wang, Z.; Zheng, S.; Li, C.; Sun, Z. The critical role of minerals in persulfate-based advanced oxidation process: Catalytic properties, mechanism, and prospects. *Chem. Eng. J.* **2024**, *482*, 148969. [CrossRef]
3. Yin, R.; Zhang, Y.; Wang, Y.; Zhao, J.; Shang, C. Far-UVC Photolysis of Peroxydisulfate for Micropollutant Degradation in Water. *Environ. Sci. Technol.* **2024**, *58*, 6030–6038. [CrossRef] [PubMed]
4. Guerra-Rodríguez, S.; Abeledo-Lameiro, M.J.; Polo-López, M.I.; Plaza-Bolaños, P.; Agüera, A.; Rodríguez, E.; Rodríguez-Chueca, J. Pilot-scale sulfate radical-based advanced oxidation for wastewater reuse: Simultaneous disinfection, removal of contaminants of emerging concern, and antibiotic resistance genes. *Chem. Eng. J.* **2023**, *477*, 146916. [CrossRef]
5. Ding, X.; Wei, C.; Wei, Y.; Liu, P.; Wang, D.; Wang, Q.; Chen, X.; Song, X. Field test of thermally activated persulfate for remediation of PFASs co-contaminated with chlorinated aliphatic hydrocarbons in groundwater. *Water Res.* **2024**, *249*, 120993. [CrossRef] [PubMed]
6. Dong, J.; Yang, P.; Chen, J.; Ji, Y.; Lu, J. Nitrophenolic byproducts formation during sulfate radical oxidation and their fate in simulated drinking water treatment processes. *Water Res.* **2022**, *224*, 119054. [CrossRef] [PubMed]
7. Chu, L.; Cang, L.; Sun, Z.; Wang, X.; Chen, H.; Fang, G.; Gao, J. Mechanism of nitro-byproducts formation during persulfate-based electrokinetic in situ oxidation for remediation of anthracene contaminated soil. *J. Hazard. Mater.* **2023**, *453*, 131396. [CrossRef] [PubMed]
8. Du, Y.; Cao, J.-Y.; Lu, Y.; Zhang, H.; Zhang, J.; Shi, Y.; Lai, B. Cytotoxicity and Genotoxicity toward Mammalian Cells Induced by Organic Iodine in Peroxymonosulfate (PMS) Processes: Activated PMS Is Better than Nonactivated PMS in Mitigating Toxicity. *Environ. Sci. Technol.* **2025**, *59*, 5925–5935. [CrossRef] [PubMed]
9. Van Buren, J.; Cuthbertson, A.A.; Ocasio, D.; Sedlak, D.L. Ubiquitous Production of Organosulfates during Treatment of Organic Contaminants with Sulfate Radicals. *Environ. Sci. Technol. Lett.* **2021**, *8*, 574–580. [CrossRef] [PubMed]
10. Li, J.; Qin, W.; Zhu, B.; Ruan, T.; Hua, Z.; Du, H.; Dong, S.; Fang, J. Insights into the transformation of natural organic matter during UV/peroxydisulfate treatment by FT-ICR MS and machine learning: Non-negligible formation of organosulfates. *Water Res.* **2024**, *256*, 121564. [CrossRef] [PubMed]
11. Kottapurath Vijay, A.; Marks, V.; Mizrahi, A.; Wen, Y.; Ma, X.; Sharma, V.K.; Meyerstein, D. Reaction of FeaqII with Peroxymonosulfate and Peroxydisulfate in the Presence of Bicarbonate: Formation of FeaqIV and Carbonate Radical Anions. *Environ. Sci. Technol.* **2023**, *57*, 6743–6753. [CrossRef] [PubMed]
12. Nihemaiti, M.; Icker, M.; Seiwert, B.; Reemtsma, T. Revisiting Disinfection Byproducts with Supercritical Fluid Chromatography-High Resolution-Mass Spectrometry: Identification of Novel Halogenated Sulfonic Acids in Disinfected Drinking Water. *Environ. Sci. Technol.* **2023**, *57*, 3527–3537. [CrossRef] [PubMed]
13. Mantzouki, C.; Mavrogianni, D.; Papagianni, M.; Konomos, G.; Creatsas, G.; Drakakis, P.; Mastorakos, G. The deleterious effect of bisphenol S on early embryo development of mice. *Hormones* **2025**, *24*, 533–542. [CrossRef] [PubMed]
14. Karbowska, M.; Pawlak, K.; Sieklucka, B.; Domaniewski, T.; Lebkowska, U.; Zawadzki, R.; Pawlak, D. Dose-dependent exposure to indoxyl sulfate alters AHR signaling, sirtuins gene expression, oxidative DNA damage, and bone mineral status in rats. *Sci. Rep.* **2024**, *14*, 2583. [CrossRef] [PubMed]
15. Braun, G.; Herberth, G.; Krauss, M.; König, M.; Wojtysiak, N.; Zenclussen, A.C.; Escher, B.I. Neurotoxic mixture effects of chemicals extracted from blood of pregnant women. *Science* **2024**, *386*, 301–309. [CrossRef] [PubMed]
16. Du, Y.; Wang, W.-L.; Wang, Z.-W.; Yuan, C.-J.; Ye, M.-Q.; Wu, Q.-Y. Overlooked cytotoxicity and genotoxicity to mammalian cells caused by the oxidant peroxymonosulfate during wastewater treatment compared with the sulfate radical-based ultraviolet/peroxymonosulfate process. *Environ. Sci. Technol.* **2023**, *57*, 3311–3322. [CrossRef] [PubMed]
17. Lai, D.; Bai, Y.; Zhang, Z.; So, P.K.; Li, Y.J.; Tse, Y.L.S.; Yeung, Y.Y.; Schaefer, T.; Herrmann, H.; Yu, J.Z.; et al. Rapid aqueous-phase oxidation of an α-pinene-derived organosulfate by hydroxyl radicals: A potential source of some unclassified oxygenated and small organosulfates in the atmosphere. *Atmos. Chem. Phys.* **2025**, *25*, 12569–12584. [CrossRef]
18. Liu, Y.; Wang, K.; Zhou, Z.; Wei, X.; Xia, S.; Wang, X.-M.; Xie, Y.F.; Huang, X. Boosting the Performance of Nanofiltration Membranes in Removing Organic Micropollutants: Trade-Off Effect, Strategy Evaluation, and Prospective Development. *Environ. Sci. Technol.* **2022**, *56*, 15220–15237. [CrossRef] [PubMed]
19. Xu, X.; Chen, Y.; Wang, Z.; Hua, G.; Zhang, Z.; Liu, S.; Jin, P.; Liu, F.; Wang, H. Nanofiltration membranes with ultra-high negative charge density for enhanced anion sieving and removal of organic micropollutants. *Nat. Water* **2025**, *3*, 704–713. [CrossRef]
20. Liu, Y.; Li, G.; Zhang, X.; Du, Z.; Zhang, T.; Zhang, Y.; Lavendomme, R.; Gao, E.-Q.; Zhang, D. A Hexadecacationic Metal–Organic Cage for Anchoring Sulfonates: High-Order Binding of Di- and Trisulfonates and High-Performance Removal of Perfluorosulfonates from Water. *Adv. Sci.* **2026**, *13*, e15258. [CrossRef] [PubMed]

21. Kato, S.; Otake, K.-i.; Chen, H.; Akpinar, I.; Buru, C.T.; Islamoglu, T.; Snurr, R.Q.; Farha, O.K. Zirconium-Based Metal–Organic Frameworks for the Removal of Protein-Bound Uremic Toxin from Human Serum Albumin. *J. Am. Chem. Soc.* **2019**, *141*, 2568–2576. [CrossRef] [PubMed]
22. Cuchiaro, H.; Thai, J.; Schaffner, N.; Tuttle, R.R.; Reynolds, M. Exploring the Parameter Space of p-Cresyl Sulfate Adsorption in Metal–Organic Frameworks. *ACS Appl. Mater. Interfaces* **2020**, *12*, 22572–22580. [CrossRef] [PubMed]
23. Li, J.; Han, L.; Xie, J.; Liu, S.; Jia, L. Multi-sites polycyclodextrin adsorbents for removal of protein-bound uremic toxins combining with hemodialysis. *Carbohydr. Polym.* **2020**, *247*, 116665. [CrossRef] [PubMed]
24. Pires, R.F.; Nunes, B.S.; Rodrigues, F.S.C.; Paul, A.; Charas, A.; Kamakar, A.; Faria, M. Incorporation of NU-1000 into cellulose acetate membranes with preserved indoxyl sulfate adsorption. *J. Mater. Chem. B* **2026**, *14*, 3743–3762. [CrossRef] [PubMed]
25. Hou, J.; Liu, M.; Gao, W.; Yan, K.; Li, B.; Zheng, W.; Gong, S.; Zhang, X.; Sun, W. Understanding the Adsorption and Diffusion Behaviors of PBUT in Biocompatible MOFs. *J. Phys. Chem. B* **2024**, *128*, 8886–8895. [CrossRef] [PubMed]
26. Qin, J.; Long, Y.; Sun, F.; Zhou, P.-P.; Wang, W.D.; Luo, N.; Ma, J. Zr(OH)4-Catalyzed Controllable Selective Oxidation of Anilines to Azoxybenzenes, Azobenzenes and Nitrosobenzenes. *Angew. Chem.* **2022**, *134*, e202112907. [CrossRef]
27. Huang, C.; Tang, Z.; Zhang, Z. Differences between Zirconium Hydroxide ($Zr(OH)_4 \cdot nH_2O$) and Hydrous Zirconia ($ZrO_2 \cdot nH_2O$). *J. Am. Ceram. Soc.* **2004**, *84*, 1637–1638. [CrossRef]
28. Frisch, M.J.; Trucks, G.W.; Schlegel, H.B.; Scuseria, G.E.; Robb, M.A.; Cheeseman, J.R.; Scalmani, G.; Barone, V.; Petersson, G.A.; Nakatsuji, H.; et al. *Gaussian 16 Rev. C.01*; Gaussian, Inc.: Wallingford, CT, USA, 2016.
29. Adamo, C.; Barone, V. Toward reliable density functional methods without adjustable parameters: The PBE0 model. *J. Chem. Phys.* **1999**, *110*, 6158–6170. [CrossRef]
30. Grimme, S.; Antony, J.; Ehrlich, S.; Krieg, H. A consistent and accurate ab initio parametrization of density functional dispersion correction (DFT-D) for the 94 elements H-Pu. *J. Chem. Phys.* **2010**, *132*, 154104. [CrossRef] [PubMed]
31. Grimme, S.; Ehrlich, S.; Goerigk, L. Effect of the damping function in dispersion corrected density functional theory. *J. Comput. Chem.* **2011**, *32*, 1456–1465. [CrossRef] [PubMed]
32. Andrae, D.; Häußermann, U.; Dolg, M.; Stoll, H.; Preuß, H. Energy-adjusted ab initiopseudopotentials for the second and third row transition elements. *Theor. Chim. Acta* **1990**, *77*, 123–141. [CrossRef]
33. Krishnan, R.; Binkley, J.S.; Seeger, R.; Pople, J.A. Self-consistent molecular orbital methods. XX. A basis set for correlated wave functions. *J. Chem. Phys.* **1980**, *72*, 650–654. [CrossRef]
34. McLean, A.D.; Chandler, G.S. Contracted Gaussian basis sets for molecular calculations. I. Second row atoms, Z=11–18. *J. Chem. Phys.* **1980**, *72*, 5639–5648. [CrossRef]
35. Marenich, A.V.; Cramer, C.J.; Truhlar, D.G. Universal Solvation Model Based on Solute Electron Density and on a Continuum Model of the Solvent Defined by the Bulk Dielectric Constant and Atomic Surface Tensions. *J. Phys. Chem. B* **2009**, *113*, 6378–6396. [CrossRef] [PubMed]
36. Zhao, Z.; Yang, G.; Wang, P.; Yue, S.; Yang, M.; Zhang, T.; Zhan, S. Regulating nonradicals generation through peroxymonosulfate activation via localized dipole to enhance wastewater biodegradability. *Nat. Commun.* **2025**, *16*, 5861. [CrossRef] [PubMed]
37. Chen, S.; Qi, Y.; Xie, Q.; Ma, C.; Zhong, S.; Wu, L.; Fu, P. Elucidating Dissolved Organic Sulfur in the Coastal Environment by Improved Online Liquid Chromatography Coupled to FT-ICR Mass Spectrometry. *J. Geophys. Res. Oceans* **2024**, *129*, e2023JC020163. [CrossRef]
38. Wang, Y.; Deng, H.; Li, P.; Xu, J.; Jiang, B.; Pang, H.; Gligorovski, S. Molecular Characterization of the Product Compounds Formed Upon Heterogeneous Chemistry of Ozone With Riverine Surface Microlayer. *J. Geophys. Res. Atmos.* **2022**, *127*, e2022JD037182. [CrossRef]
39. Andersson, P.G. A Note on Confidence Intervals for a Binomial p: Andersson–Nerman vs. Wilson. *Stat* **2024**, *13*, e70027. [CrossRef]
40. Koch, B.P.; Dittmar, T. From mass to structure: An aromaticity index for high-resolution mass data of natural organic matter. *Rapid Commun. Mass Spectrom.* **2016**, *30*, 250. [CrossRef]
41. Hu, J.; Kang, L.; Li, Z.; Feng, X.; Liang, C.; Wu, Z.; Zhou, W.; Liu, X.; Yang, Y.; Chen, L. Photo-produced aromatic compounds stimulate microbial degradation of dissolved organic carbon in thermokarst lakes. *Nat. Commun.* **2023**, *14*, 3681. [CrossRef] [PubMed]
42. Meissel, K.; Yao, E.S. Using Cliff's delta as a non-parametric effect size measure: An accessible web app and R tutorial. *Pract. Assess. Res. Eval.* **2024**, *29*, 2.
43. Zhao, C.; Wang, C.; Wang, Z.; Wang, B.; Yao, G.; Qiu, Y.; Yang, R. Study of the removal of Pb(ii) and Ni(ii) from aqueous solution by new nano-$Mg(OH)_2$/fly ash adsorbent materials. *New J. Chem.* **2023**, *47*, 10952–10966. [CrossRef]
44. Ramachandran, S.; Kappl, M.; Sperling, M.; Gradzielski, M.; Butt, H., Jr. Fabrication of Janus Supraparticles by Induced Phase Separation by Gravity. *ACS Nano* **2026**, *20*, 12285–12295. [CrossRef] [PubMed]
45. Huang, X.; Auffan, M.; Eckelman, M.J.; Elimelech, M.; Kim, J.-H.; Rose, J.; Zuo, K.; Li, Q.; Alvarez, P.J.J. Trends, risks and opportunities in environmental nanotechnology. *Nat. Rev. Earth Environ.* **2024**, *5*, 572–587. [CrossRef]

46. Zha, S.; Liu, H.; Li, H.; Li, H.; Wong, K.-L.; All, A.H. Functionalized Nanomaterials Capable of Crossing the Blood–Brain Barrier. *ACS Nano* **2024**, *18*, 1820–1845. [CrossRef] [PubMed]
47. Cho, Y.; Seo, E.U.; Hwang, K.S.; Kim, H.; Choi, J.; Kim, H.N. Evaluation of size-dependent uptake, transport and cytotoxicity of polystyrene microplastic in a blood-brain barrier (BBB) model. *Nano Converg.* **2024**, *11*, 40. [CrossRef] [PubMed]
48. Celeste, A.; Paolone, A.; Itié, J.-P.; Borondics, F.; Joseph, B.; Grad, O.; Blanita, G.; Zlotea, C.; Capitani, F. Mesoporous Metal–Organic Framework MIL-101 at High Pressure. *J. Am. Chem. Soc.* **2020**, *142*, 15012–15019. [CrossRef] [PubMed]
49. Maiorov, D.V.; Yakovlev, K.A. Synthesis Method Influence on the Physicochemical Properties and Phase Composition of Zirconium Dioxide. *Glass Ceram.* **2022**, *79*, 210–217. [CrossRef]
50. Ruzimuradov, O.; Braglia, M.; Vacandio, F.; Knauth, P. A humidity-sensitive nanocomposite solid ion conductor: Sulfonated poly-ether-ether-ketone in nanotubular TiO_2 or ZrO_2 matrix. *J. Solid State Electrochem.* **2018**, *22*, 3255–3260. [CrossRef]
51. Shun, K.; Mori, K.; Masuda, S.; Hashimoto, N.; Hinuma, Y.; Kobayashi, H.; Yamashita, H. Revealing hydrogen spillover pathways in reducible metal oxides. *Chem. Sci.* **2022**, *13*, 8137–8147. [CrossRef] [PubMed]
52. Wu, W.; Li, N.; Che, C.; Zhao, J.; Qin, J.; Feng, Z.; Song, J.; Zhang, Z.; Zhang, R.; Long, Y. $Zr(OH)_4$-Catalyzed Semi-Hydrogenation of Phenylacetylene with Terminal Zr−O−H as Active Site: Inactive for Free Styrene. *Angew. Chem. Int. Ed.* **2024**, *63*, e202410246. [CrossRef] [PubMed]
53. Su, P.; Tang, J.; Wu, M.; Guo, X.; Zhang, C.; Guo, Q.; Liu, Z.; Li, J.; Zhang, J. Enhanced sulfate adsorption in mine water via Fe-Zr bimetal modified ginkgo leaf-derived biochar: Mechanistic insights and DFT calculations. *Sep. Purif. Technol.* **2025**, *376*, 133941. [CrossRef]
54. Xia, P.; Yang, C.; Wang, X.; Jian, J.; Liang, L.; O'Carroll, D.M.; He, F. Facet-dependent adsorption of PFOS and 6:2 Cl-PFESA onto hematite surfaces. *Environ. Pollut.* **2026**, *407*, 128770. [CrossRef] [PubMed]
55. Morton, K.S.C.; Malley, A.J.O.; Armstrong, J. Probing adsorption interactions of lignin derivatives in industrial zeolite catalysts through combining vibrational spectroscopy and ab initio calculations. *RSC Sustain.* **2025**, *3*, 2938–2951. [CrossRef]
56. Lee, J.J.; Son, H.G.; Jeong, K.; Roh, S.B.; Kwon, S.; Kim, S.M.; Seo, J.H.; Kim, P.S.; Choi, J.; Park, J.H. The Potential of Methyl Groups: Can Methyl Groups Unlock Reactivity Limitations of the Acceptorless Dehydrogenation of N-Heterocycles? *JACS Au* **2025**, *5*, 3339–3349. [CrossRef] [PubMed]
57. Nihemaiti, M.; Wullenweber, J.; Stefanoni, M.; Kahle, L.; Lechtenfeld, O.J.; Cantoni, B.; Antonelli, M.; Ernst, M.; Reemtsma, T. Formation of regulated and novel disinfection by-products during chlorine and chlorine dioxide disinfection of surface water and groundwater. *Water Res.* **2026**, *290*, 124996. [CrossRef] [PubMed]
58. Javanmardi, A.J.; Plassmann, M.; Mathew, A.P. Concomitant Removal of Perfluorooctanoic Acid (PFOA) and Humic Acid from Water Using a Cationic Cellulose Nanofiber. *ACS Omega* **2026**, *11*, 31588. [CrossRef] [PubMed]
59. Nakahata, M.; Sumiya, A.; Ikemoto, Y.; Nakamura, T.; Dudin, A.; Schwieger, J.; Yamamoto, A.; Sakai, S.; Kaufmann, S.; Tanaka, M. Hyperconfined bio-inspired Polymers in Integrative Flow-Through Systems for Highly Selective Removal of Heavy Metal Ions. *Nat. Commun.* **2024**, *15*, 5824. [CrossRef] [PubMed]
60. Ma, Q.; Mu, J.; Lv, X.; Meng, J.; Cui, H.; Qiu, Y.; Ruan, H.; Shen, J. Sustainable Recovery of Ionic Resources from Resin Regeneration Wastewater: Long-Term Evaluation, Membrane Fouling Analysis, and Cleaning. *ACS EST Water* **2023**, *3*, 1855–1864. [CrossRef]
61. Fang, Y.; Meng, P.; Schaefer, C.; Knappe, D.R.U. Removal and destruction of perfluoroalkyl ether carboxylic acids (PFECAs) in an anion exchange resin and electrochemical oxidation treatment train. *Water Res.* **2023**, *230*, 119522. [CrossRef] [PubMed]

Disclaimer/Publisher's Note: The statements, opinions and data contained in all publications are solely those of the individual author(s) and contributor(s) and not of MDPI and/or the editor(s). MDPI and/or the editor(s) disclaim responsibility for any injury to people or property resulting from any ideas, methods, instructions or products referred to in the content.